Numerical study of unsteady pipe flow of an elastoviscoplastic fluid

Miguel Moyers-González, Cathy Castelain, Teodor Burghelea

Numerical study of Unsteady Pipe Flow of an Elastoviscoplastic Fluid

Miguel Moyers-González[a,*], Cathy Castelain[b], Teodor Burghelea[b]

[a]*School of Mathematics and Statistics, University of Canterbury. Private Bag 4800, Christchurch, 8140, New Zealand*
[b]*Nantes Université, CNRS, Laboratoire de Thermique et Énergie de Nantes, LTeN, UMR 6607, F-44000, Nantes, France*

Abstract

In this paper we investigate, numerically, unsteady Poiseuille flow of an elastoviscoplastic fluid. The material is described by the rheological model by Putz and Burghelea [1]. The model can describe an elastic solid regime for low stresses, a solid-fluid phase of stresses in the vicinity of the yield stress and a fully fluid regime for large stresses. We impose a time dependent pressure ramp with the form of a triangular function to drive the flow. We compare average velocity across the pipe as a function of pressure drop for different slip laws. We find that the solid-fluid transition is correlated to the slip-law used in the computations but the boundary conditions do not affect neither the deformation-rates nor stress at the bulk and the wall.

Keywords: Unsteady Flow, Elastoviscoplastic, Slip law.

1. Introduction

A broad class of materials exhibit a dual response when subjected to an external stress. For low applied stresses they behave as solids (loosely speaking they may deform but no macroscopic flow is observed) but, if the stress exceeds a critical threshold generally referred to as the *"yield stress"*, they behave as fluids (typically non-Newtonian) and a macroscopic flow is observed. This distinct class of materials has been termed as *"yield stress materials"* and, during the past several decades it attracted a constantly increasing level of interest from both theoreticians and experimentalists. The motivation behind this increasing level of interest is two-fold. From a practical standpoint, such materials have found a significant number of applications in several key industries (which include food, cosmetics, pharmaceutical, oil field engineering, etc.) and they are encountered in daily life in numerous forms such as food pastes, hair gels and emulsions, cement, mud etc.. More recently, hydrogels which exhibit a yield stress have found a number of future promising applications including targeted drug delivery [2, 3], contact lenses, noninvasive intervertebral disc repair [4] and tissue engineering [5].

From a fundamental standpoint, yield stress materials continue triggering intensive debates and posing difficult challenges to both theoreticians and experimentalists from various communities: soft matter physics, rheology, physical chemistry and applied mathematics. The progress in understanding the flow behaviour of yield stress materials made the object of several review papers [6, 7, 8, 9]. The best known debate concerning the yield stress materials is undoubtedly that related to the very existence of a "true" yield stress behaviour [10, 11]. During the past two decades, however, a number of technical improvements of the rheometric equipment made possible measurements of torques as small as $0.1n\ Nm$ and of rates of deformation as small as $10^{-7}\ s^{-1}$). Such accurate rheological measurements proved unequivocally the existence of a true yielding behaviour [1, 12, 13]. The physics of the yielding process itself on the other hand remains elusive. The macroscopic response of yield stress fluids subjected to an external stress σ has been classically described by the Herschel-Bulkley model [14, 15]:

$$\sigma = \sigma_y + K\dot{\gamma}^n \tag{1}$$

*Corresponding author
Email address: miguel.moyersgonzalez@canterbury.ac.nz (Miguel Moyers-González)

Here σ_y is the yield stress, $\dot{\gamma}$ is the rate of shear, i.e., the rate at which the material is being deformed, σ is the macroscopically applied stress (the external forcing parameter), K is a so-called consistency parameter that sets the viscosity scale in the flowing state and n is the power law index which characterises the degree of shear thinning of the viscosity beyond the yield point.

Materials that have a yield-stress are known to slip when the vessel where they are being deformed has a smooth surface, [16]. In his seminal work, Navier [17] was the first to propose a slip model where the velocity at the wall is linearly proportional to the wall shear stress:

$$u_w = \beta \tau_w \tag{2}$$

where β is the slip coefficient and it is related to the width of the slip layer. Evidence of a non-linear relation between slip velocity and wall shear stress has driven researchers, see [18, 19, 20, 21], to generalise Navier's law to a power-law type of model of the form:

$$u_w = \beta (\tau_w)^m. \tag{3}$$

Experimental evidence of a "stick-slip" behaviour has been found for several materials under different flow conditions, see [20, 22, 23, 24, 25]. In this model, slip only occurs when a Columbic type of friction term called *slip yield stress* is exceeded at the wall. Several authors have proposed different ways to model this "stick-slip" condition.

In [20] Hatzikiriakos and Dealy used a Bingham type equation for the slip velocity

$$u_w = \begin{cases} \alpha \tau_w^m & \tau_w > \tau_{y,w} \\ 0 & \tau_w \leq \tau_{y,w}, \end{cases} \tag{4}$$

where $\tau_{y,w}$ is the slip yield stress. Equivalent formulations to 4 have been used by several groups for analytical and numerical investigations, see [26, 27, 28]. In [29], Roquet and Saramito proposed a continuous version of (4):

$$u_w = -\max\left(0, \beta - \frac{\tau_{y,w}}{|\tau_w|}\right) \tau_w. \tag{5}$$

Here β is the reciprocal of a friction dissipation coefficient. In this work we consider and equivalent formulation of (5).

Flows involving slip have been studied for decades. For this work we concentrate in studies that involved flows with a stick-slip law or viscoplastic fluids with slip at the wall. Georgious and Kaoullas, [27, 28] studied Poiseuille flow of a Newtonian fluid in a square and triangular ducts with stick-slip law at the wall. Depending on the value of the pressure drop applied they describe different flow regimes. For axisymmetric flow two regimes exist, slip along all the boundary above and no slip at the wall. When the symmetry condition is broken, one extra regime can be found, only in a partial section of the boundary the wall shear stress exceeds the slip yield stress.

Poiseuille flows of viscoplastic materials in a square duct with a stick-slip law were first investigated by Roquet and Saramito in [29]. They found that depending on the ratio between slip yield stress and bulk yield stress (S) and the intensity of the pressure drop the flow can be characterised in the following way: i) If $S < 0.7$, the flow may be arrested, the fluid moves as a rigid solid (block translation) and flow in the bulk while full slip at the wall. ii) Similarly, if $0.7 \leq S \leq 1$ there is a no flow regime, flow in the bulk with partial slip at the wall and flow in the bulk with total slip at the wall. iii) When $S > 1$, we have the same regimes as in (ii) with the addition of a regime between no flow and flow with partial slip, flow in the bulk with no slip at the wall.

Damianou and Georgiou studied viscoplastic Poiseuille flow in a rectangular duct with wall slip in [30] and found similar results as in the square duct case of Roquet and Saramito [29].

Yoshimura and Prud'homme, were the first model model unsteady pipe flows of a Bingham fluid with an elastic solid core following Hooke's law [31]. Similar studies concerning with different flow configurations and forcing have been reported recently, [32, 33]. However, a systematic analysis of the coupling between the

solid-fluid transition and the wall slip behaviour typically observed in experiments is, to our best knowledge, missing. This sets the global scope of the present contribution.

2. Elastoviscoplastic model with internal microstructure

Prior to discussing the elasto-viscoplastic model, we will briefly recall several key rheological features of the physical gel used in the experiments reported in Ref. [16]. The material used was an aqueous solution of Carbopol 980 neutralised by adding the right amount of sodium hydroxide. The details of the procedure used to prepare the gel sample are given in Ref. [16]. The macro-rheological characterisation of the solution was performed using a commercial rotational rheometer (Mars III from Thermofischer scientific) equipped with nano-torque module. The instrumental accuracy of the device is roughly $0.5nN\ m$ for the torque measurements and $10^{-5}\ s^{-1}$ for the shear rate. We have used a plate plate geometry with a gap $d = 1\ mm$. To prevent the wall slip during the rheological tests, both plates have been covered with sand-paper and the inertia of the geometry re-calibrated. To test the absence of wall slip effects, we have repeated the measurements for several values of the gap d and found no visible difference.

As a protocol, we have used an increasing/decreasing controlled stress stepped ramp as shown in Fig. 1(a) and defined by:

$$\sigma(t) = \sigma_{max} \frac{-2N + 1 + \sum_{k=0,t_0}^{N} H(t-k) + \sum_{k=N+1,t_0}^{2N} H(k-t)}{N} \tag{6}$$

Here H stands for the Heaviside step function, t_0 is the duration of each step (to be further referred to as the *"characteristic forcing time"*) of the ramp and $T_{max} = N\ t_0$ is the total duration of the loading/unloading branches of the ramp. As we are interested in case of unsteady forcing, the characteristic forcing time was rather small, $t_0 = 5\ s$ (see the inset in Fig. 1(a)). The largest value of the applied stress σ_{max} has been chosen such as the entire material was yielded. A representative result of such test is presented in Fig. 1(b). The error bars have been obtained by repeating the rheological test three times.

The rheological response of the material to such an unsteady forcing is illustrated in Fig. 1(b) which presents the dependence of the absolute value of the rate of shear $|\dot{\gamma}|$ on the applied stress σ. Several important features of the response of the Carbopol gel to the unsteady forcing already highlighted and systematically reproduced in several subsequent papers [1, 34, 35, 36, 37, 38, 39, 40, 41] can be noted as follows:

1. The transition from an elastic solid regime **(S)** that can be described by the Hooke's law $\sigma = G\gamma$ (where γ is the strain) to a fully fluidised regime **(F)** that can be accurately described by the Herschel-Bulkley law given by Eq. 1 (the dotted line in Fig. 1(b)) is not direct but mediated by an intermediate deformation regime **(S+F)** where the solid and the purely viscous behaviours coexist.
2. The solid fluid transition is reversible upon increasing/decreasing control parameter (the externally applied stress stress) only within the fluid deformation regime **(F)**. Within the solid and solid-fluid coexistence regime **(S+F)** a clear hysteresis is observed. This type of irreversible behaviour has been observed for a number of chemically different yield stress materials, [35] which indicates that it is rather universal. The magnitude of the hysteresis or the power per unit volume of material that is not recovered upon the loading/unloading of the sample decays algebraically with the characteristic forcing time t_0, [1]. Thus, in the asymptotic limit of steady forcing $t_0 \to \infty$, the Carbopol gels do recover their status of *"model"* yield stress materials.
3. On the decreasing branch of the controlled stress ramp (the full symbols in Fig. 1(b)) an elastic recoil is observed in the form of a cusp marked by a full red circle. At this point, the rate of deformation becomes negative, i.e. the sense of rotation of the rheometer shaft is reversed.

Although Carbopol gels have been considered *"model"* yield stress fluids, the features enumerated above indicate that this is not entirely the case as they exhibit both a weak thixotropic behaviour and some elasticity around the onset of the solid-fluid transition.

However, this conclusion is still subjected to a fair amount of controversy within the viscoplastic community. Recently, Dinkgreve and her coworkers have argued that these weakly thixotropic effects solely occur if the Carbopol gel is over-stirred during the preparation (more precisely during the neutralisation phase) which, according to them, results in an irreversible damage of its microstructure leading to an irreversibility of the deformation states, [42]. In an even more recent paper, however, it is demonstrated just the contrary: gently stirred (during the neutralisation phase) Carbopol gels still exhibit the weakly thixotropic and elastic behaviour highlighted above, [41] (see Fig. 2(a) therein). A second very important claim made in Ref. [42] is that the thixotropic behaviour of the over-stirred Carbopol (particularly the hysteresis behaviour) can be modelled by the simple λ - model proposed by Coussot and co-workers, [43] (see Fig. 7 in Ref. [42]). A first counter-proof of this claim is trivial: thixotropic or not, any Carbopol gels exhibits a shear-thinning behaviour beyond the yield point while the λ - model predicts a constant (Newtonian) viscosity far above the yield point. We are simply not aware of any experimental paper that shows a constant viscosity of a Carbopol gel in a fully yielded state. The second counter proof relates to the fact that the λ - model has no elasticity embedded whereas it is common knowledge that, prior to the solid-fluid transition, Carbobol gels behave as Hookean solids. To conclude this part, contrary to what is shown in Fig. 7 of Ref. [42], the flow curve of a Carbopol gel can not be described by the simple λ - model.

To describe the yielding behaviour of a Carbopol gel we will resort to the phenomenological model proposed in [1, 37]. The flow of an elastovisplastic fluid is described by the following set of equations with unknowns $(p, \boldsymbol{u}, \boldsymbol{\tau}, \Phi)$:

$$\rho\left(\frac{\partial \boldsymbol{u}}{\partial t} + (\boldsymbol{u}\cdot\boldsymbol{\nabla})\boldsymbol{u}\right) = -\nabla p + \boldsymbol{\nabla}\cdot\boldsymbol{\tau} \tag{7}$$

$$\boldsymbol{\nabla}\cdot\boldsymbol{u} = 0, \tag{8}$$

where $\boldsymbol{u}$ is the velocity field, p the pressure, and $\boldsymbol{\tau}$ is the stress tensor. The constitutive equation for the model is:

$$\boldsymbol{\tau} + \lambda(\dot{\gamma}, \Phi)\, \overset{\triangledown}{\boldsymbol{\tau}} = \mu\left(\dot{\gamma}(\boldsymbol{u})\right)\dot{\boldsymbol{\gamma}}, \tag{9}$$

where

$$\overset{\triangledown}{\cdot} = \frac{D\cdot}{Dt} - \boldsymbol{\nabla}\boldsymbol{u}\cdot - \cdot\boldsymbol{\nabla}\boldsymbol{u}^T$$

is the Upper-Convected-Derivative, $D\cdot/Dt$ is the usual material derivative,

$$\lambda(\dot{\gamma}, \Phi) = \frac{\mu\left(\dot{\gamma}(\boldsymbol{u})\right)}{G}\Phi$$

is the relaxation time, G is the elastic modulus, and $\dot{\boldsymbol{\gamma}} = \dot{\boldsymbol{\gamma}}(\boldsymbol{u})$ is rate of strain tensor.

Finally, the concentration of the solid state, Φ, satisfies the following kinematic equation:

$$\frac{\partial \Phi}{\partial t} + (\boldsymbol{u}\cdot\boldsymbol{\nabla})\Phi = R_d(\Phi, \tau(\boldsymbol{u})) + R_r(\Phi, \tau(\boldsymbol{u})), \tag{10}$$

with R_d being the rate of destruction of solid units and R_r is the rate of fluid recombination of fluid elements into a gelled structure.

Note that when $\Phi \equiv 1$ the model describes a White-Metzner viscoelastic fluid and if $\Phi \equiv 0$ the model represents a Generalized Newtonian fluid.

In both (9) and (10), $\dot{\gamma}$ and τ are the second invariant of the rate of strain and stress tensors respectively. These are defined as follow:

$$\dot{\gamma}(\boldsymbol{u}) = \left(\frac{1}{2}\sum_{i,j=1}^{3}[\dot{\gamma}_{ij}(\boldsymbol{u})]^2\right)^{1/2}, \qquad \tau(\boldsymbol{u}) = \left(\frac{1}{2}\sum_{i,j=1}^{3}[\tau_{ij}(\boldsymbol{u})]^2\right)^{1/2}.$$

2.1. Choice of functions for nonlinear viscosity, destruction rate and recombination rate.

The choices for the nonlinear viscosity $\mu(\dot{\gamma})$ and the destruction and recombination rate functions are presented below. We note that the choices are clearly non unique in this type of phenomenological models. The description of the rates of destruction and recombination is rather empirical. However, it has been shown both qualitatively and quantitatively from first principles that the choices for destruction and recombination functions presented in [1, 37] can describe a yield stress material [38, 44, 39] . Below we present the full model.

2.1.1. Non-linear viscosity $\mu(\dot{\gamma})$

The fluids we are interested in present a yield stress. As discussed in Sec. 2, the transition from an elastic solid behaviour (unyielded) to a fluid behaviour (yielded) is not direct but mediated a regime where solid and fluid behaviour coexist **(S+F)**. Given the fact that in our case yielding is a smooth process we choose as viscosity function the regularised Herschel-Bulkley model:

$$\mu(\dot{\gamma}) = \left(\kappa\dot{\gamma}^{n-1} + \frac{\tau_y(1-\exp(-m\dot{\gamma})}{\dot{\gamma}}\right), \tag{11}$$

where κ is the consistency of the material, $n < 1$ is the power law index, and τ_y is the yield stress and $m \gg 1$ is the regularisation parameter.

2.1.2. R_d and R_r

As in [1, 37] we have:

$$R_d(\Phi, \tau(\boldsymbol{u})) = -g(\tau(\boldsymbol{u}))\Phi, \tag{12}$$

with

$$g(\tau(\boldsymbol{u})) = K_d\left(1 + \tanh\left(\frac{\tau(\boldsymbol{u}) - \tau_y}{w}\right)\right), \tag{13}$$

and

$$R_r(\Phi, \tau(\boldsymbol{u})) = f(\tau(\boldsymbol{u}))(1-\Phi), \tag{14}$$

with

$$f(\tau(\boldsymbol{u})) = K_r\left(1 - \tanh\left(\frac{\tau(\boldsymbol{u}) - \tau_y}{w}\right)\right). \tag{15}$$

Here K_d and K_r are the rate of destruction and rate of recombination with units s^{-1}, w determines the width of the solid-fluid region and has units Pa.

The model reduces to:

$$\frac{d\Phi}{dt} = -g(\tau)\Phi + f(\tau)(1-\Phi), \tag{16}$$

$$\frac{\mu(\dot{\gamma})}{G}\Phi\frac{d\tau}{dt} + \tau = \mu(\dot{\gamma})\dot{\gamma}. \tag{17}$$

In order to find the best set of parameters that accurately fit the controlled stress ramps data with the model presented above, we have written a nested function program in Matlab. The main function uses the built-in function *lsqnonlin* which solves nonlinear least-squares fitting problems using a trust-region-reflective algorithm. As input we provide an initial guess for the parameters vector, the target data (see the symbols in Fig. 1(b)) and a function which first solves the equation 16 for Φ using the built-in function *ode15s* in Matlab and then solves Eq. 17 for $\dot{\gamma}$ using the built-in function *fzero* in Matlab. The output of the main function is a vector with the optimal parameter values. We note that we fitted the increasing/decreasing branches of the flow ramp were fitted separately in order to properly capture the hysteresis behaviour visible in Fig. 1(b) within the **(S)** and **(S+F)** deformation regimes. The best fitting functions obtained according to this procedure are shown in Fig. 1(b) as full lines.

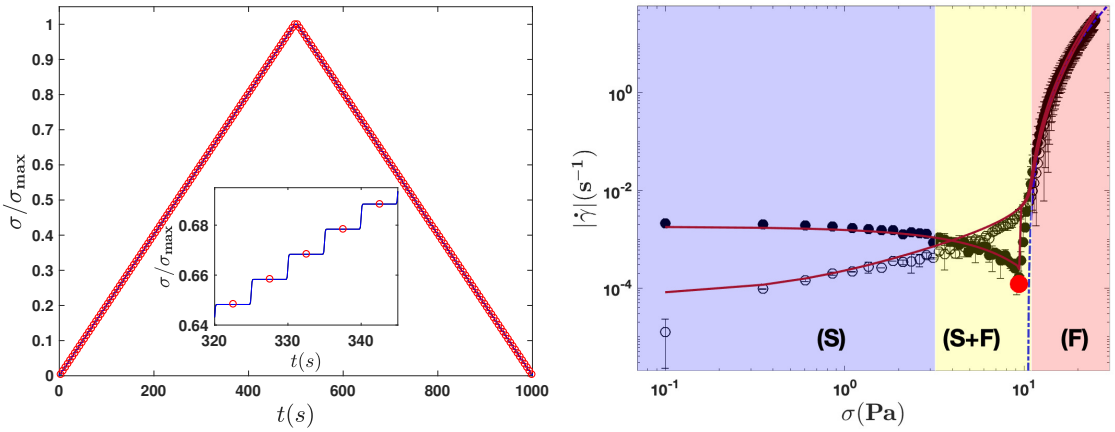

Figure 1: 1(a) Controlled stress ramp used for the rheological characterisation of the gel. The characteristic forcing time is $t_0 = 5\ s$. The inset presents a magnified view. 1(b) Dependence of the modulus of the shear rate $|\dot{\gamma}|$ on the applied stress σ measured for increasing/decreasing stresses, empty/full symbols respectively. The dotted line is a Hereschel-Bulkley fit according to Eq. (1). The full symbol marks the point when an elastic recoil is observed ($\dot{\gamma}$ changes sign). The full lines are the best fit obtained using the elasto-viscoplastic model. The symbols **(S)**, **(F)** stand for solid, fluid respectively.

The fitting functions shown in Figure 1(b) confirm that we can fully reproduce all the main features of the unsteady rheological behaviour quite accurately. Note that when $\tau < \tau_y$ $\mu(\dot{\gamma}) \gg 1$, and by dominant balance, equation (17) approximates the definition of a viscoelastic solid.

Due to its ability to fit very well the response during loading/unloading ramps, we will resort to this model later through the paper in order to describe the laminar unsteady pipe flow with various wall slip conditions.

3. Problem description

As already stated in the Introduction, we numerically approximate the unsteady flow of an elasto-viscoplastic fluid in a circular pipe at low Reynolds number and compare the results with the experimental findings reported in Ref. [16]. The experiments were performed in a glass tube with a circular cross-section and a radius $R = 1.9\ mm$ and a length $L = 115\ cm$.

The unsteady flows are driven by a pressure drop varying in time as schematically illustrated in Fig. 2(a). This unsteady forcing scheme closely mimics the stepped stress ramp used during the rheological tests discussed in Sec. 2. The experiments were performed for several values of the time per pressure step t_0 ranging from 4 s to 15 s.

We illustrate in Fig. 2(b) time averaged transversal profiles of the axial velocity measured for the largest value of t_0 corresponding to a steady state (the data is replotted from Fig. 4(c) of Ref. [16]). Here U_s stands for the slip velocity, U_p stands for the velocity of the rigid plug located around the centre-line of the tube and U_{av} is the velocity averaged across the channel. As we are in the case of a steady forcing (large t_0), the transverse profiles of the time averaged velocity are reproducible upon increasing/decreasing the pressure drop consistently with a reversible flow regime (the full and empty symbols in Fig. 2(b) overlap). The reproducibility of the velocity profiles in the steady state limit is consistent with the power law decay of the hysteresis of the rheological flow curves with respect to the characteristic forcing time t_0, [1].

The velocity profiles displayed in Fig. 2(b) are consistent with the theoretical picture of a laminar and steady flow behaviour of a viscoplastic fluid in a tube. Following [45] and in the framework of the

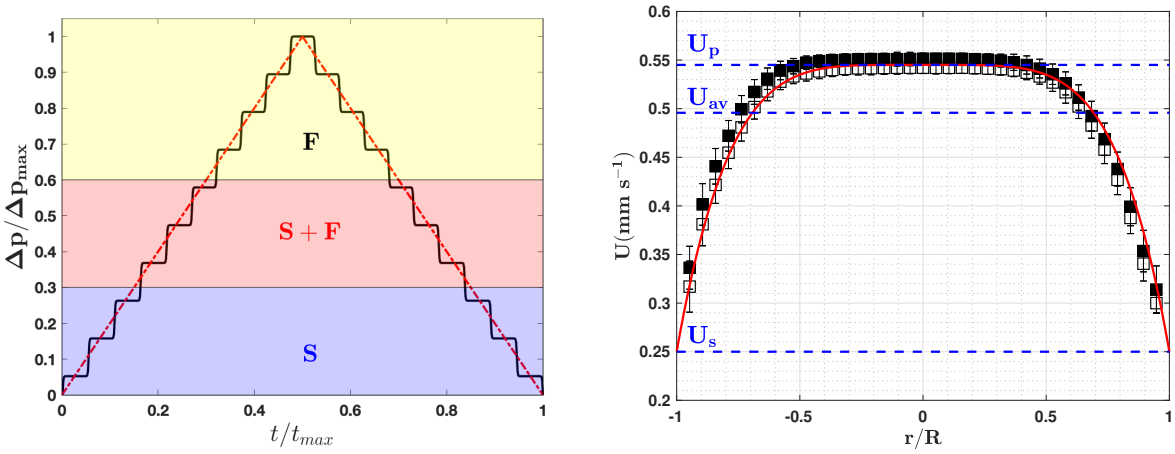

Figure 2: 2(a) The controlled pressure ramp used to generate the unsteady flows studied in Ref. [16]. The characteristic forcing time was $t_0 = 5\ s$. 2(b) Example of steady state transversal profiles of the time averaged axial velocity measured for both increasing (full symbols) and decreasing (empty symbols) driving pressures Δp. The solid red curve corresponds to (18).

Herschel-Bulkley model the steady state velocity profile can be formally [1] fitted by (the full line in Fig. 2(b)):

$$U(r) = U_s + \left(\frac{n}{n+1}\right)\left(\frac{1}{2K}\cdot\frac{\Delta p}{L}\right)^{\frac{1}{n}}(R-R_p)^{\frac{1}{n}+1}\left[1-\left(\frac{r-R_p}{R-R_p}\right)^{\frac{1}{n}+1}\right] \tag{18}$$

Here R_p is the radius of the un-yielded plug. The slip velocity was measured by either extrapolating the fit given by Eq. (18) at the wall when a reliable fit could be obtained (i.e. at larger driving pressures when the viscoplastic profile is developed) or by extrapolation of a spline interpolation function.

3.1. Non-dimensionalisation

We have unsteady unidirectional flow hence, we non-dimensionalise our equations as follow:

$$r = \hat{r}R,\ z = \hat{z}L,\ t = \hat{t}t_c,\ \boldsymbol{u} = \hat{\boldsymbol{u}}u_c,\ p = \hat{p}\frac{\Delta pR}{\rho u_c^2},\ \boldsymbol{\tau} = \hat{\boldsymbol{\tau}}\kappa\left(\frac{u_c}{R}\right)^n.$$

From our experimental results we can see that the right characteristic scale for time is the "yielding" time which we define $t_c = \dot{\gamma}_c^{-1}$, hence the natural characteristic velocity scale is then defined as $u_c = \dot{\gamma}_c * R$.

The scaling for the physical parameters in (10) is:

$$K_d = \hat{K}_d\dot{\gamma}_c^{-1},\ K_r = \hat{K}_r\dot{\gamma}_c^{-1},\ w = \hat{w}\kappa\left(\frac{u_c}{R}\right)^n.$$

Substituting all this into equations (7)-(10) and dropping hats for simplicity we have our unsteady one dimensional problem:

[1] Note that the slip term U_s is not accounted for in [45] which discusses the slip-free case and has been formally added here to describe the measured transverse velocity profiles.

$$\frac{\partial u}{\partial t} = -\frac{dp}{dz} + \frac{1}{Re}\frac{1}{r}\frac{}{\partial r}(r\tau_{rz}) \tag{19}$$

$$We\mu(\dot{\gamma})\Phi\frac{\partial \tau_{rz}}{\partial t} + \tau_{rz} = \mu(\dot{\gamma})\frac{\partial u}{\partial r} \tag{20}$$

$$We\mu(\dot{\gamma})\Phi\frac{\partial \tau_{zz}}{\partial t} + \tau_{zz} = 2We\mu(\dot{\gamma})\Phi\tau_{rz}\frac{\partial u}{\partial r} \tag{21}$$

$$\frac{d\Phi}{dt} = -g(\tau)\Phi + f(\tau)(1-\Phi) \tag{22}$$

where

$$\dot{\gamma} = \left|\frac{\partial u}{\partial r}\right| \quad , Re = \frac{\rho u_c R}{\eta}, \quad We = \frac{\eta u_c}{RG} \quad \text{and} \quad \eta = \kappa\left(\frac{u_c}{R}\right)^{n-1}$$

Here

$$\mu(\dot{\gamma}) = \left(\dot{\gamma}^{n-1} + \frac{B(1-\exp(-m\dot{\gamma})}{\dot{\gamma}}\right)$$

$$g(\tau) = K_d\left(1 + \tanh\left(\frac{\tau - B}{w}\right)\right)$$

$$f(\tau) = K_r\left(1 - \tanh\left(\frac{\tau - B}{w}\right)\right)$$

with

$$B = \frac{\tau_y R}{u_c \eta} \quad \text{and} \quad \tau = \left(\frac{1}{2}(\tau_{zz}^2 + 2\tau_{rz}^2)\right)^{1/2}$$

and boundary condition at the wall,

$$u = F(\tau_w).$$

Note that $F(\tau_w)$ can be equal to zero in the case of no-slip condition.

3.2. Boundary conditions

In [16], the authors showed that flow irreversibility is strongly coupled with wall slip. Even though they propose a non-linear Navier-slip law to model the behaviour at the wall, they acknowledge that due to the non-negligible level of scatter of their data more investigation in order to describe the relation between flow properties, wall slip and microstructure is needed. Hence, for the rest of the paper we consider four different boundary conditions (no-slip/slip laws).

3.2.1. Slip Laws

For all our numerical simulations, we will consider the following cases at $r = 1$.

- No slip (NS)

$$u_w = 0. \tag{23}$$

- Navier slip (S1)

$$u_w = \beta\tau_{rz,w}. \tag{24}$$

- Power law Navier slip less than one (S2), [21]

$$u_w = \beta\tau_{rz,w}^{1/3}. \tag{25}$$

- Power law Navier slip greater than one (S3), [16]

$$u_w = \beta\tau_{rz,w}^{3/2}. \tag{26}$$

- Continuous "stick-slip" law (S4), [29]

$$u_w = \max\left(0, 1 - \frac{B_w}{|\tau_{rz,w}|}\right)\beta\tau_{rz,w}. \tag{27}$$

where

$$B_w = \frac{\tau_{y,w}R}{U\eta}$$

is the slip Bingham number and $\tau_{y,w}$ is the slip yield stress.

4. Numerical method

Equations (19)-(22) are discretised using a second order finite difference scheme in space and a first order implicit scheme in time. We assume symmetry of our velocity profile and solve for $r \in [0, 1]$. The nonlinear system is presented below:

$$\frac{u_i^j - u_i^{j-1}}{\Delta t} = f(t_i) + \frac{1}{Re}\frac{1}{r_{i+1/2}}\left(\frac{r_{i+1}\tau_{rz,i+1}^j - r_i\tau_{rz,i}^j}{2\Delta r}\right) \tag{28}$$

$$We_k\mu_i^j\Phi_i^j\left(\frac{\tau_{rz,i}^j - \tau_{rz,i}^{j-1}}{\Delta t}\right) + \tau_{rz,i}^j = \mu_i^j\left(\frac{u_{i+1}^j - u_{i-1}^j}{2\Delta r}\right) \tag{29}$$

$$We_k\mu_i^j\Phi_i^j\left(\frac{\tau_{zz,i}^j - \tau_{zz,i}^{j-1}}{\Delta t}\right) + \tau_{zz,i}^j = 2We_k\mu_i^j\Phi_i^j\tau_{rz,i}^j\left(\frac{u_{i+1}^j - u_{i-1}^j}{2\Delta r}\right) \tag{30}$$

$$\frac{\Phi_i^j - \Phi_i^{j-1}}{\Delta t} = K_r\left(1 - \tanh\left(\frac{\tau_i^j - B}{w}\right)\right)(1 - \Phi_i^j) - K_d\left(1 + \tanh\left(\frac{\tau_i^j - B}{w}\right)\right)\Phi_i^j \tag{31}$$

with symmetry condition at $r = 0$ and one of (23)-(27) at $r = 1$.

We solve the system of nonlinear equations (28)-(31) using a fixed-point algorithm at each time step. For all our calculations we set $\Delta r = 5 \times 10^{-3}$ and $\Delta t = 10^{-5}$. As we start from a quiescent state, all our initial conditions are zero at $t = 0$.

5. Results

For all the simulations presented below we use the following parameter values in agreement with the parameters that refer to the experiments reported in Ref. [16]: $R = 1.9$mm, $L = 1.15$ m, $\rho = 990$ kg/m^3, $\kappa = 0.118$ Pas^{-n}, $\tau_y = 0.65$ Pa, $\tau_{y,w} = 0.2$ Pa, $G_{up} = 100$ Pa, $G_{down} = 20$ Pa, $n = 0.77$, $\Delta p = 3000$ Pa, $\dot{\gamma}_c = 0.02$ s^{-1}, $u_c = 3.8 \cdot 10^{-5}$ m/s, $t_c = 1/\dot{\gamma}_c = 50$ s and $\hat{\beta} = 5 \cdot 10^{-5}$ m/(Pas)^a. The regularisation parameter for the viscosity function is fixed at $m = 500$. Note that here $a = 1/3,\ 1,\ 3/2$ depending which slip law we choose. For simplicity we use the same value for $\hat{\beta}$ for all slip cases. For most of our results we fix our forcing time $\hat{t}_0 = 2$ s.

Hence our nondimensional parameters are: $Re = 2.4634 \times 10^{-5}$, $We_{up} = 5.8033 \times 10^{-5}$, $We_{down} = 2.9017 \times 10^{-4}$, $B = 112.0052$, $B_w = 34.4631$, $m = 500$, $K_r = 20$, $K_d = 1$, $w = 0.1$ and $\beta = 0.076$ and $t_0 = 0.04$.

In Figure 3 we present the absolute value of the velocity averaged along the transversal flow direction as a function of pressure drop Δp. This is allows us to directly compare the response of the material to the unsteady pressure forcing in the tube with the macro- rheological response to the unsteady loading/unloading. In the absence of slip at the wall (the curve denoted by $\circ$), the dependence is qualitatively similar to that obtained from macro-rheological measurements illustrated in Fig 1(b). For low values of Δp the velocity is almost constant for both the increasing and the decreasing branch of the pressure ramp which is clear

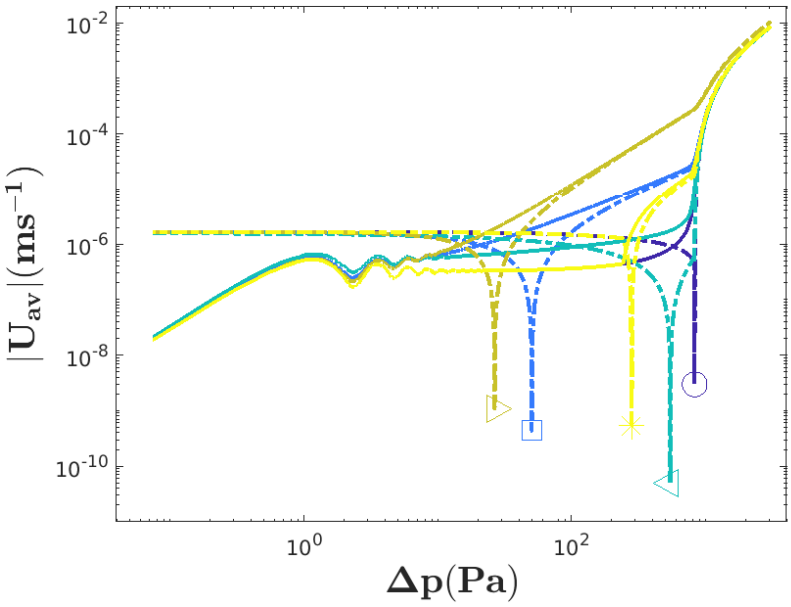

Figure 3: Dependence of the average velocity U_{av} on the driving pressure drop Δp for several slip conditions: ∘ -NS, □ -S1, ◁ -S2, ▷ S3. Symbols mark the instant where U_{av} changes sign.

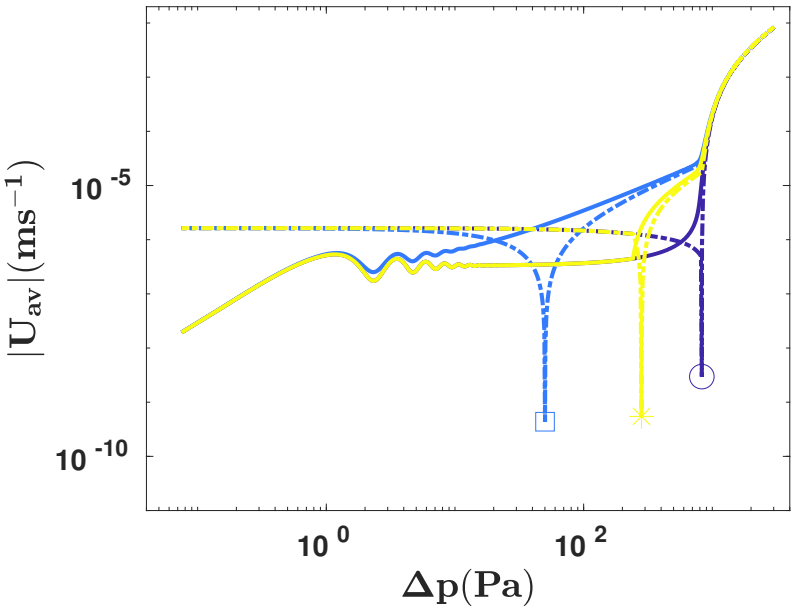

Figure 4: U_{av} vs Δp. NS-∘ and S4-∗. Symbols mark the instant where U_{av} changes sign.

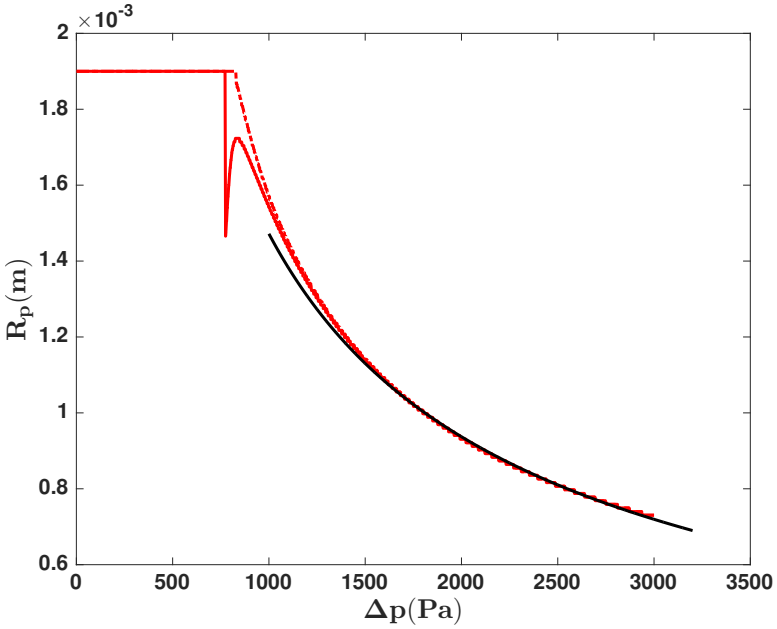

Figure 5: Dependence of the plug radius R_p on the driving pressure drop for increasing (broken line) and decreasing (full line) Δp. The black full line is the analytical solution according to the Herschel-Bulkley model, $R_p = 2L\tau_y\Delta p^{-1}$.

signature of full plug flow. For very small values of the pressure drop corresponding to the start up to the flow transient elastic effects are visible.

As the pressure drop is gradually increased, the flow fully develops. For large values of Δp the material behaves as a shear thinning fluid. Note that for non-slip and slip laws (24)-(27) we get the same response of the material for $\Delta p \leq 10$Pa and for $\Delta p \geq 900$Pa. The main difference between the no slip and slip cases is observed within the solid-fluid transition region. This indicates a direct coupling between the solid-fluid transition and the slip behaviour. For slip laws (24)-(26) the dependence of the average speed on the driving pressure follows a power law. An inflexion point is present at the boundary of the solid-fluid and fluid regions. This dependence is more evident as the exponent in the slip law increases and is fully consistent with the macro-rheological measurements (see Fig. 3(a) in Ref. [16]). As in the macro-rheological experiments, the presence of wall slip leads to a shift of the solid-fluid transitional region towards lower values of the control parameter. We note that for the "stick-slip" law (S4), this power-law behaviour in the solid-fluid region is broken. To clearly demonstrate this we plot the results for (NS), (S1) and (S4) in Figure 4.

On a closer inspection, we may identify two distinct transitions when the slip law given by Eq. (27) is used. For values of Δp up to 200 Pa the fluid behaves as a Hookean solid. When the wall shear stress exceeded the slip yield stress we get a non-linear relationship between the pressure drop and the velocity. This can be easily explained if we consider now our slip coefficient β as a function of the wall shear stress, i.e.

$$\beta_{s4}(|\tau_{rz,w}|) = \beta \max\left(0, 1 - \frac{B_w}{|\tau_{rz,w}|}\right). \tag{32}$$

Once we exceed the bulk yield stress the material behaves like a fluid and no clear difference between the no slip and slip cases can be observed which is once more qualitatively consistent with both the macro-rheological observations reported in Ref. [1] and the pipe flow experiments reported in [16].

Our simulations allow us to assess the extent of the central plug region. In Figure 5 we present the dependence of the plug size R_p on the driving pressure drops Δp. We chose to use Eq. (24) as slip law but we note that the results are almost indistinguishable for all the slip laws we have considered through the

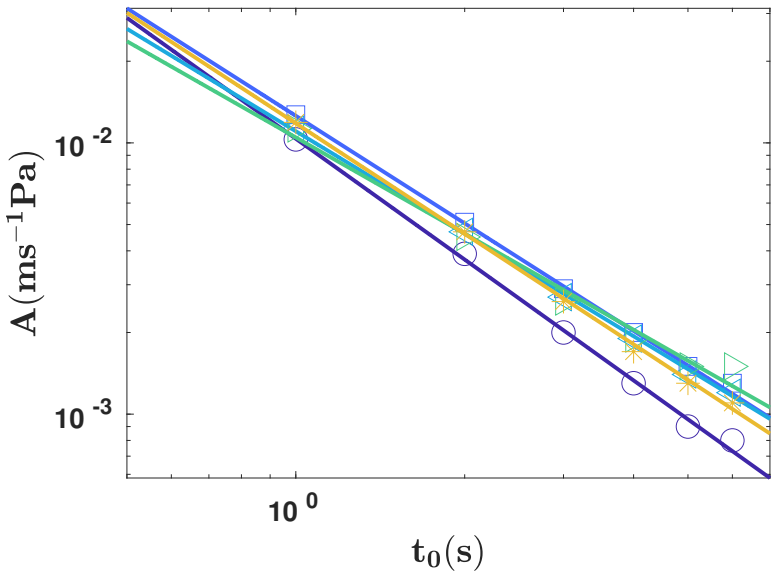

Figure 6: Hysteresis Area vs t_0. NS-$\circ$, S1-$\square$, S2-$\triangleleft$, S3-$\triangleright$ and S4-$*$

paper. In order to compute the size of plug R_p we find the region of our domain in which $\dot{\gamma} < \dot{\gamma}_c = 1/t_c$. For low values of Δp this condition is satisfied over the entire domain, hence we have a rigid body downstream motion of the material. As soon as the yield stress is overcome near the wall the plug size decreases and the solid material no longer fills the whole pipe. In the up ramp we see that the plug has not a monotonic decay for moderate values of the pressure drop, R_p increases until it reaches a local maximum and then monotonically decreases like Ax^{-m} with $m = 0.67$. The increase of the plug size could be related to the stored elastic forces. Corresponding to the decreasing branch of the pressure ramp we observe a monotonic decrease in R_p until the yielded material fills the pipe entirely. Within the transitional region, the dependence of the pus size on the driving pressure drop is irreversible upon increasing/decreasing control parameter. This irreversibility of the flow states originates into the irreversibility of the rheological flow curves illustrated in Fig. 1(b) and discussed in Sec. 2.

An intrinsic feature of the solid-fluid bifurcation undergone by a yield stress material subjected to a gradually increasing external forcing (e.g. the applied stress) is the emergence of a hysteresis of the deformation states: generally, the loading/unloading deformation curves do not coincide within the transitional region. Carbopol gels have been considered for over a decade a *model yield stress fluids* exhibiting a fully reversible solid-fluid transition (no hysteresis of the deformation states that is practically no thixotropic effects), [46]. Yet, as recently demonstrated by the experiments presented in Ref. [16], Carbopol gels may also exhibit a (relatively) weak thixotropic behaviour depending on the manner they are subjected to an external forcing. Namely, a key feature not accounted for in the afore-mentioned classification is the steadiness of the forcing i. e. the characteristic forcing time t_0. While unsteadily forced (small values of t_0) even Carbopol gels may exhibit a weakly thixotropic behaviour. In the asymptotic limit of steady forcing $t_0 \to \infty$ the magnitude of the hysteresis of the deformation states decays algebraically to 0 and the *"model"* yield stress behaviour is recovered, [1]. A more fundamental understanding of the emergence of the hysteresis behaviour has been achieved only recently, [38, 44, 39]. For the case of steady forcing, the hysteresis behaviour emerges only when the level of interactions among the molecular constituents of the material exceeds a certain threshold which is physically analogous to the Curie temperature of a magnetic system, [39]. As Carbopol gels are neutral and thus weakly interactive at a molecular scale, no hysteresis is observed during steady-state rheological tests which is consistent with the rheological measurements presented in Ref. [1] and a large body of previous studies. However, in the case of an unsteady forcing, a hysteresis behaviour will be observed

regardless the magnitude of the molecular scale interactions. Consistently with this theoretical picture, the laminar unsteady pipe flow experiments reported in Ref. [16] revealed a clear hysteresis behaviour with a magnitude weakly decaying with the characteristic forcing time t_0. The decay exponent of the hysteresis area was, however, significantly smaller than the unitary value obtained from the unsteady rheometric tests described in Ref. [1]. It was conjectured in Ref. [16] that this difference originates from the presence of wall slip during the unsteady pipe flow experiments which was absent during the rheometric tests.

To test this, we plot the area of the hysteresis vs forcing time with $t_0 = 1,\ 2,\ 3,\ 4,\ 5,\ 6$ for no-slip and all the slip laws in Fig. 6. As we can see, the area of the hysteresis decays as a power law as we increase the forcing time. The highest power corresponds to the no-slip case following a trend $A \propto t_0^{-1.48}$. We have then in order S1 to S3 with the following values $A \propto t_0^{mh}$ with $mh = -1.3168,\ -1.2549,\ -1.1776$ respectively. For the "stick-slip" case we have $mh = -1.3533$. In experimental results presented in Ref. [16] we have seen that having slip at the wall has the effect to greatly reduce the decay of the area of the hysteresis with respect of forcing time. This does not happen with the current model and slip laws. Considering slip at the wall certainly reduces the value of the exponent but clearly the model predicts a totally reversible steady state as $t_0 \to \infty$. This is inherited from equation (22). In the case of viscometric flow, our dynamical system does not go through a bifurcation. We have only one stable fixed point for Φ which lies between zero and 1. In the solid region we approximate a Hookean solid but never actually reach that state. We believe that in order to weaken the dependence between the area of the hysteresis and the forcing time a modification of the microstructure parameter equation is needed.

To further investigate the effects the slip-laws have on the flow we present in Figures 7 to 11 velocity profiles (U vs r) and micro-structure parameter profiles (Φ vs r). The rows in the figures correspond to different values of the pressure drop Δp. In the first row we consider $\Delta p = 96$Pa which corresponds to the solid regime in Figure 2(a)a. In the second and third rows we set $\Delta p = 996$Pa (solid+fluid) and $\Delta p = 3000$Pa (fluid). For all figures the forcing time is set to $t_0 = 2$s. The full line corresponds to the increasing part of pressure ramp and the broken line corresponds to the decreasing part. In all cases, see panels (a-b), for $\Delta p = 96$Pa we observe back flow on the decreasing branch of the controlled pressure ramp and hence, the model accurately predicts irreversible flow when $|\tau| \leq \tau_y$. This is confirmed in panels (b) where we show the microstructure parameter. As we can see, on the up ramp the material is fully structured whereas in the down ramp it has not have time to fully recombine itself and we have $\Phi < 1$ near the wall. In panels (c-d) and (e-f) of all figures we plot the averaged velocity and microstructure profiles computed for $\Delta p = 996$Pa and $\Delta p = 3000$Pa respectively. In panels (c-d) we are just before recoil happens and we can see the early stages of the irreversible flow, this is where the solid-fluid phase of the materials coexist. Note how in the down ramp the material takes longer to reconstitute itself, a clear signature of hysteretic behaviour. In panels (e-f) the material behaves like a shear-thinning fluid, the flow is fully reversible upon increasing/decreasing pressures and we have weaker viscoelasticity.

At first glance, we see that the shape of the velocity and microstructure parameter profiles remains the same for all boundary conditions. Not surprisingly, the only difference is a translation of the velocity profiles which is governed by the law chosen at the wall. This explains why the point at which the back flow starts is different for all boundary conditions. On the other hand, the microstructure remains unchanged for all slip laws even though the irreversibility is present. This implies that stresses and deformation-rates must remain the same irrespectively of the boundary conditions we impose. We can see that this is indeed the case in Figure 12. In figure 12a we plot the absolute value of averaged shear-stress versus the averaged shear-rate and similarly, in figure 12b, we present results of $|\dot{\gamma}_w|$ vs $|\tau_w|$ for all slip-laws. Not surprisingly, all curves collapse into one. An explanation might be that for this type of axisymmetric flow configuration, the deformation-rates and stresses are dictated only by the bulk rheological constitutive relation and are independent of what happens at the wall. Experimental results in [16] show that slip and macro-rheological characterisation of a material are interconnected (flow curves and area of the hysteresis), hence in order to accurately model this behaviour (for analytical/numerical studies), we need either a different constitutive equation or a modified slip law.

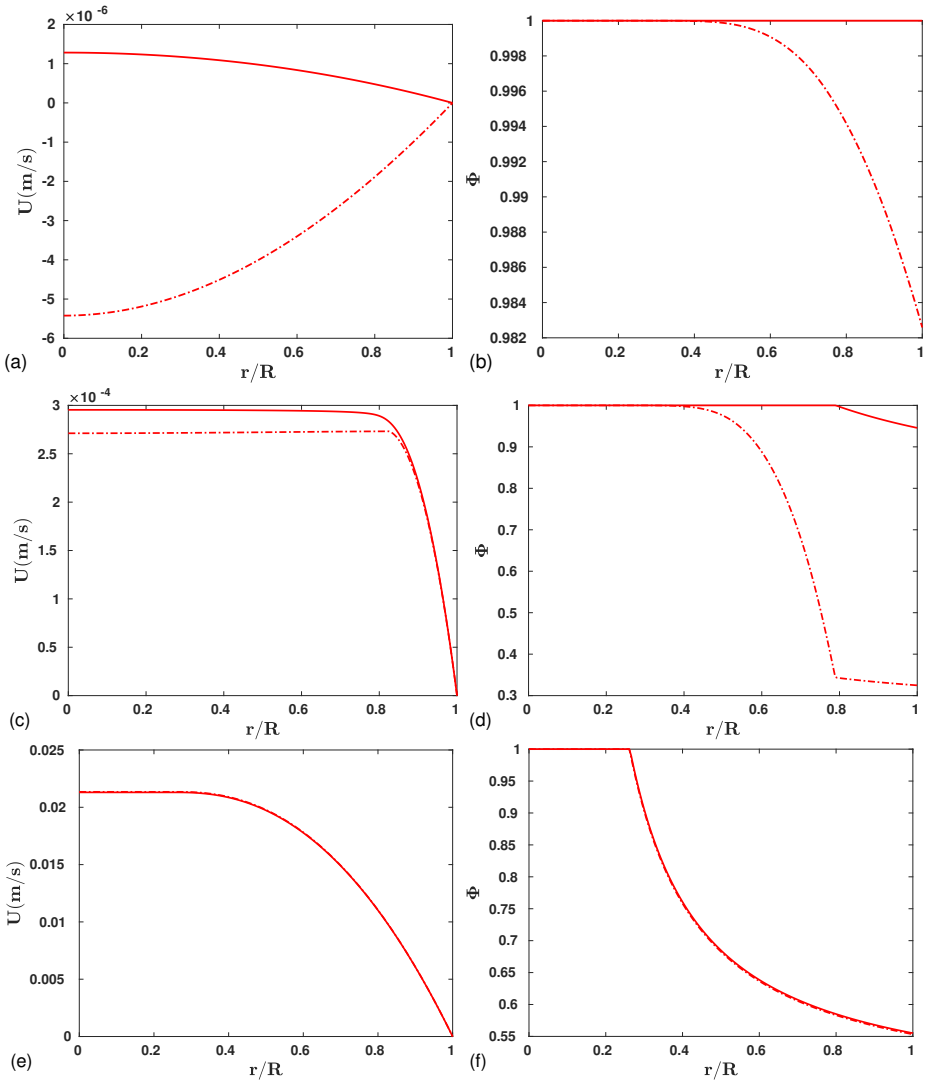

Figure 7: Velocity profiles (U) and micro-structure parameter (Φ) computed in the absence of wall slip for different values of the driving pressure Δp - (a) $\Delta p = 96\ Pa$, (b) - $\Delta p = 996\ Pa$, (c) - $\Delta p = 3000\ Pa$. Broken lines correspond to the up-ramp and full lines correspond to the down-ramp of the pressure drop.

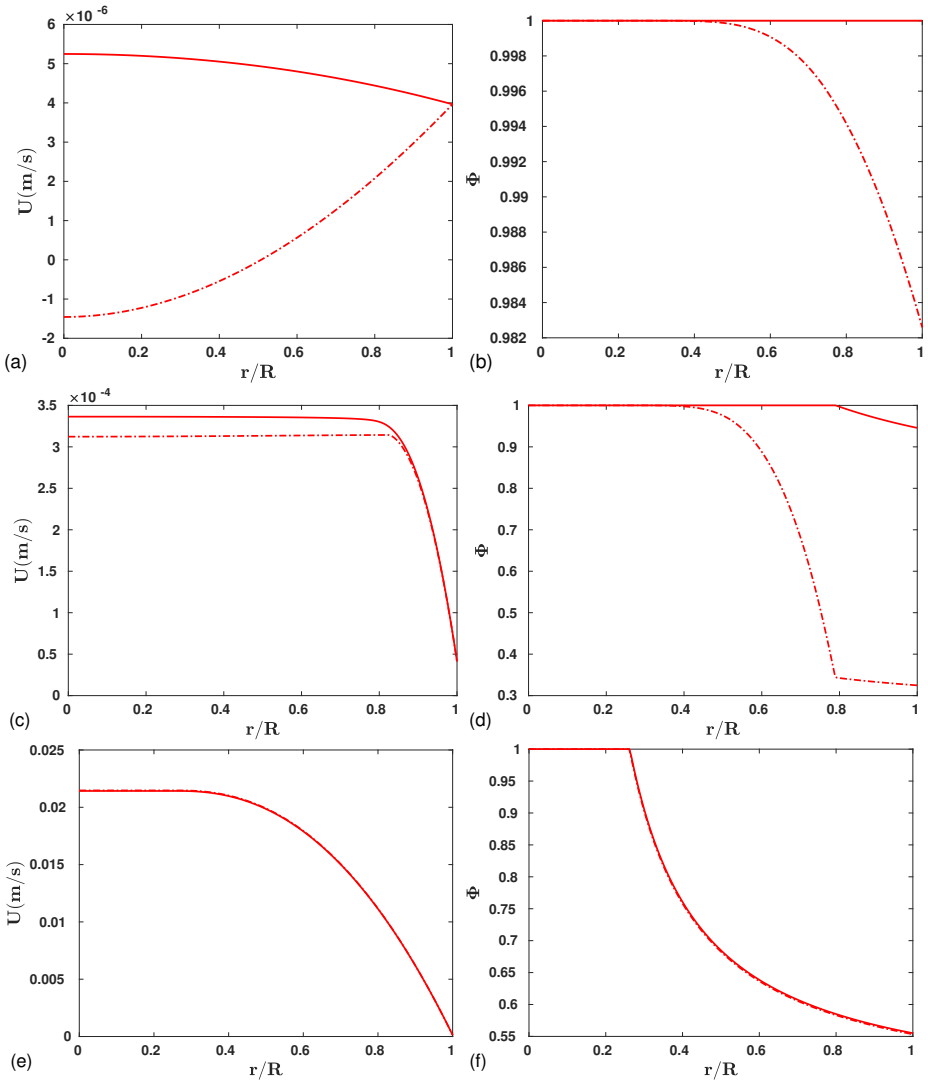

Figure 8: Velocity profiles (U) and micro-structure parameter (Φ) computed for slip-law S1 (equation (24) for different values of the driving pressure Δp - (a) $\Delta p = 96\ Pa$, (b) - $\Delta p = 996\ Pa$, (c) - $\Delta p = 3000\ Pa$. Broken lines correspond to the up-ramp and full lines correspond to the down-ramp of the pressure drop.

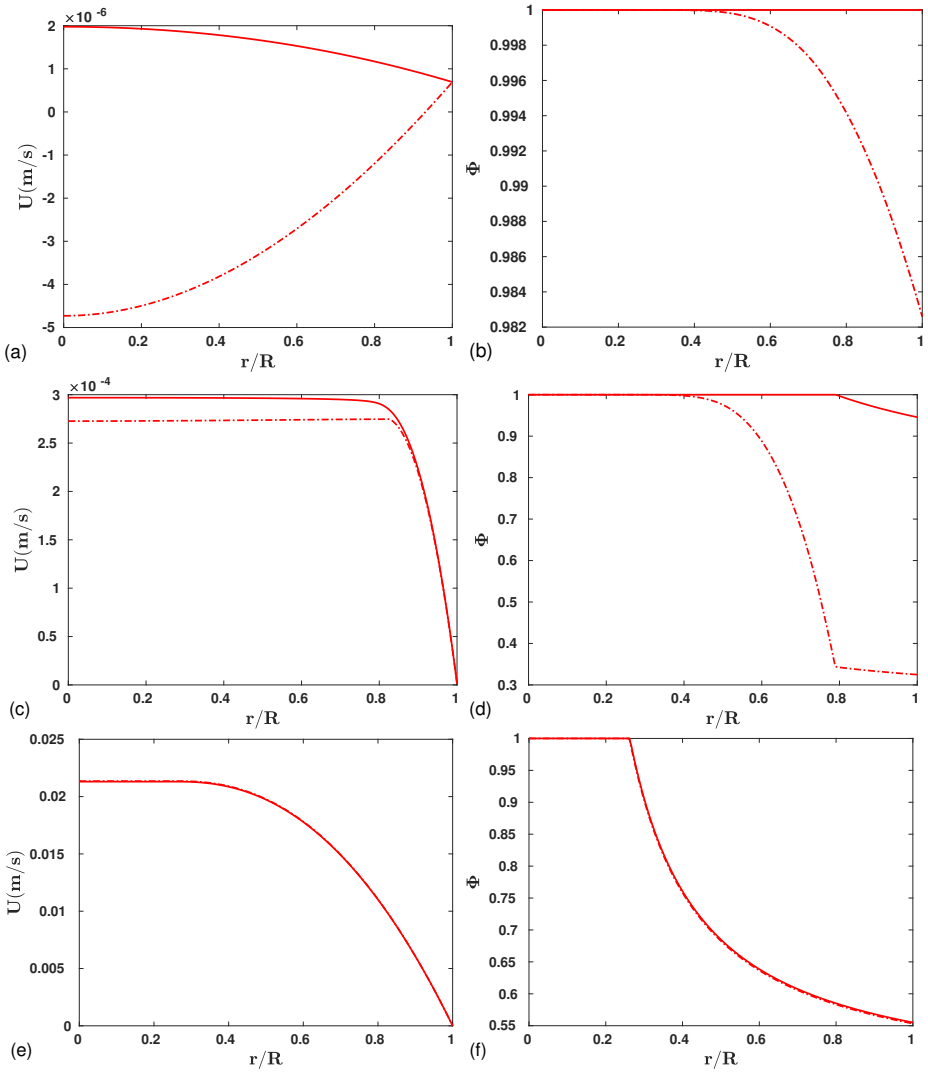

Figure 9: Velocity profiles (U) and micro-structure parameter (Φ) computed for slip-law S1 (equation (25) for different values of the driving pressure Δp - (a) $\Delta p = 96\ Pa$, (b) - $\Delta p = 996\ Pa$, (c) - $\Delta p = 3000\ Pa$. Broken lines correspond to the up-ramp and full lines correspond to the down-ramp of the pressure drop.

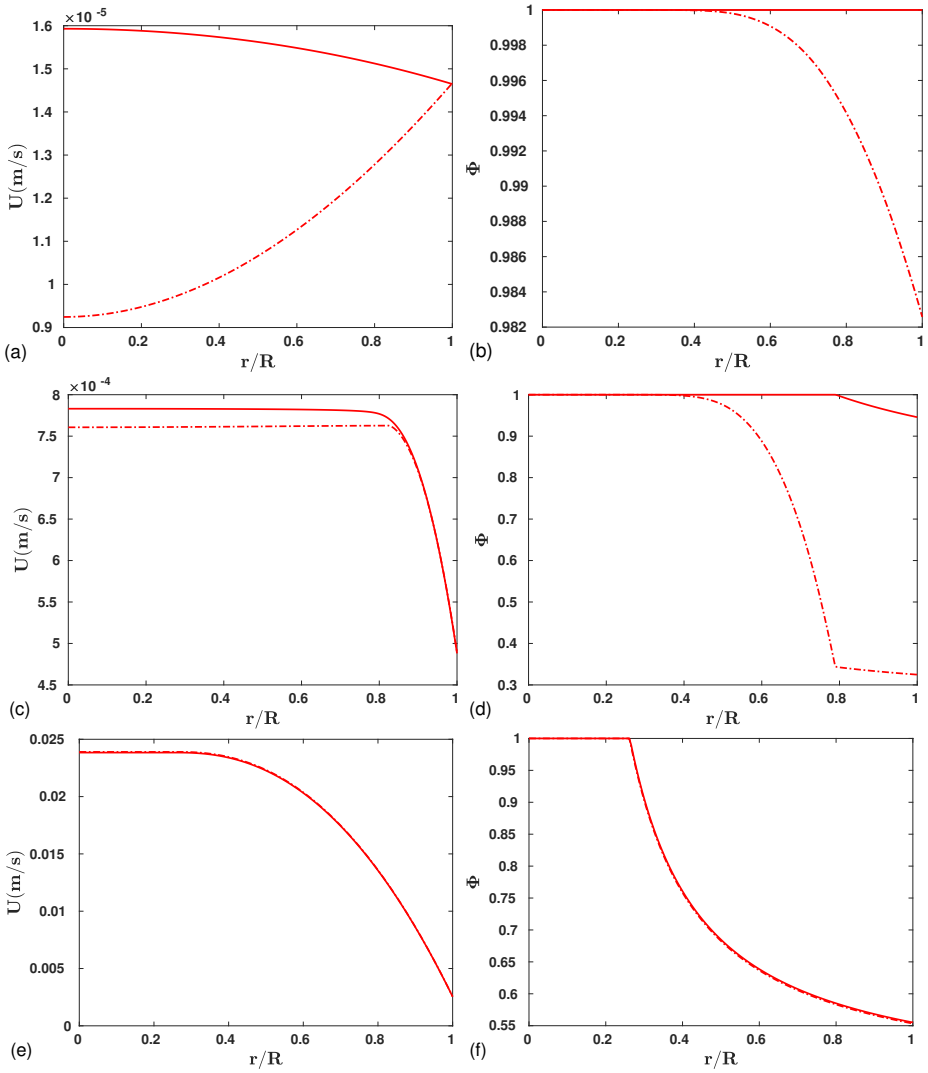

Figure 10: Velocity profiles (U) and micro-structure parameter (Φ) computed for slip-law S1 (equation (26) for different values of the driving pressure Δp - (a) $\Delta p = 96\ Pa$, (b) - $\Delta p = 996\ Pa$, (c) - $\Delta p = 3000\ Pa$. Broken lines correspond to the up-ramp and full lines correspond to the down-ramp of the pressure drop.

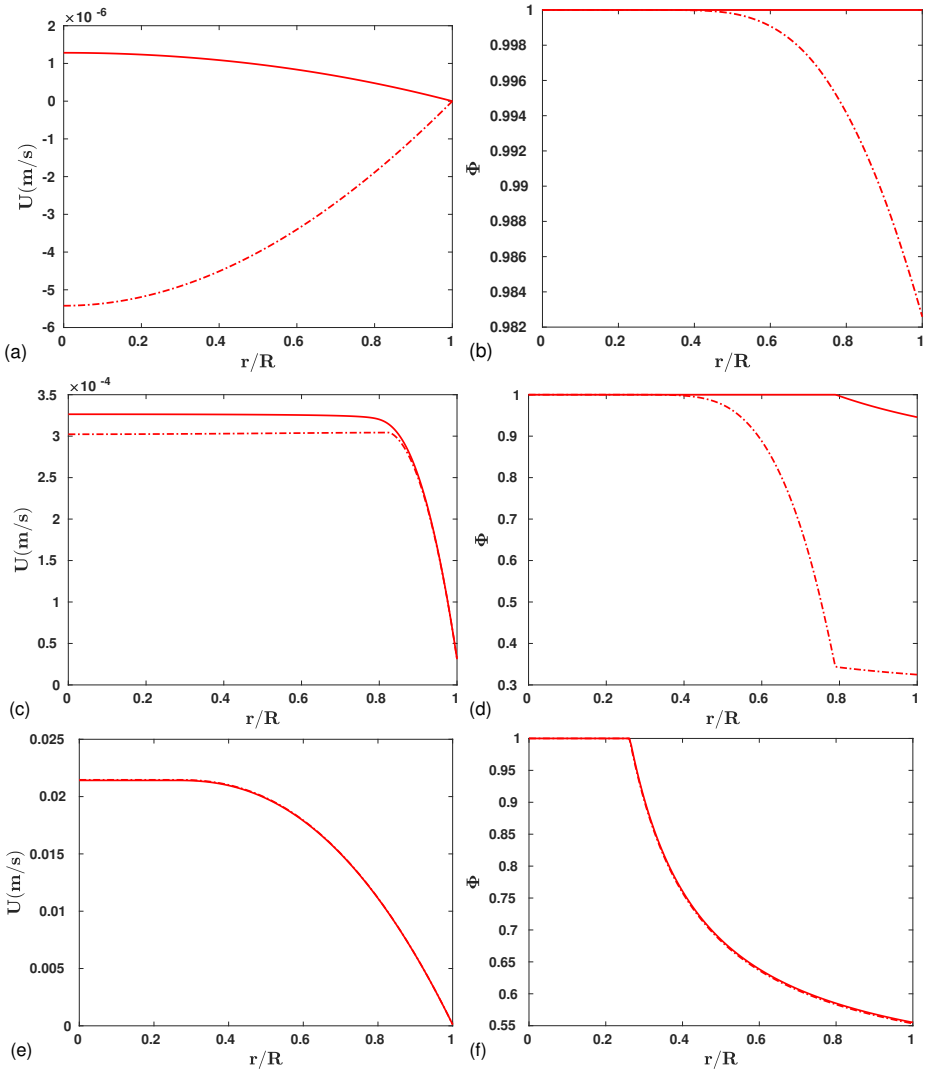

Figure 11: Velocity profiles (U) and micro-structure parameter (Φ) computed for slip-law S1 (equation (27) for different values of the driving pressure Δp - (a) $\Delta p = 96\ Pa$, (b) - $\Delta p = 996\ Pa$, (c) - $\Delta p = 3000\ Pa$. Broken lines correspond to the up-ramp and full lines correspond to the down-ramp of the pressure drop.

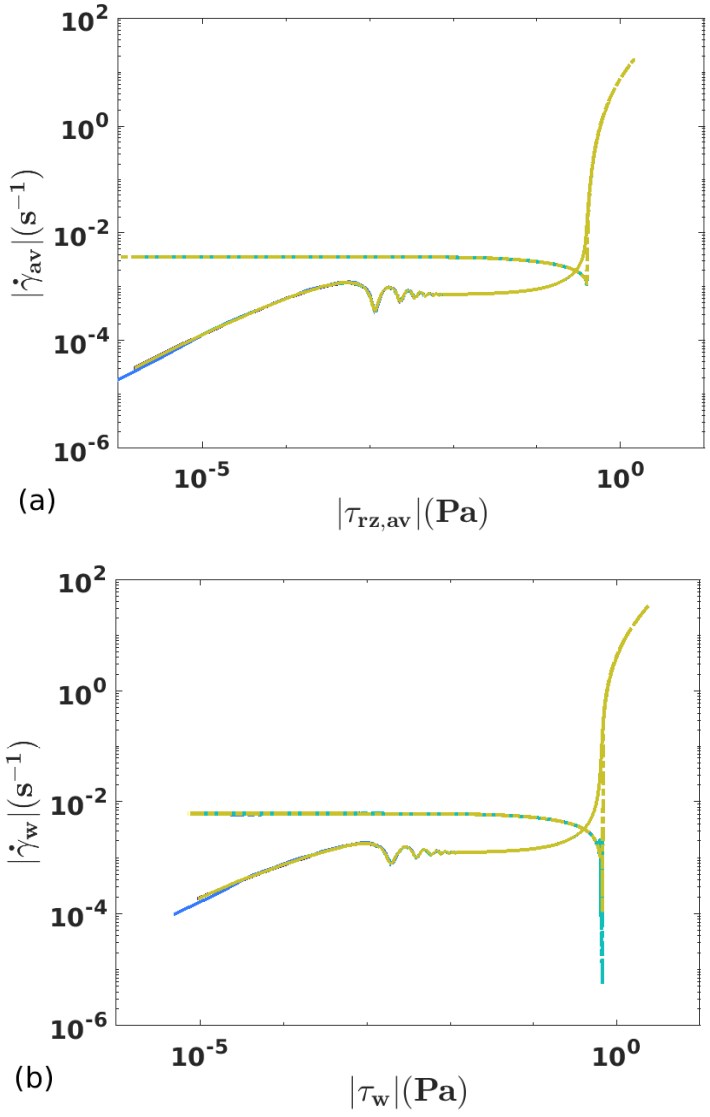

Figure 12: Shear-rate vs Shear-stress for all cases. (a) τ_{av} vs $\dot{\gamma}_{av}$. (b) τ_w vs $\dot{\gamma}_w$.

6. Conclusions

We have considered unsteady pipe flow of an elastoviscoplastic material driven by an up-down pressure ramp. Previous experimental results showed that slip at the wall allows the material to remain thixotropic, i.e. hysteresis in the flow curve is present in steady flow conditions. In our numerical results we explore several slip-laws found in the literature together with a no-slip condition. We found that in an averaged velocity and pressure map the solid-fluid transition is correlated to the law used at the wall. This is clear in figures 3 and 4 where the point at which we have back-flow is shifted by the slip-law. We can also see that, as expected, the power-law relation between U_{av} and Δp in the solid-fluid transition is solely described by the exponent in boundary conditions (24)-(26). For the stick-slip condition (27) we loose this power law behaviour, below the slip-yield stress the material sticks and as soon as the stress is above this threshold but under the bulk yield stress the material has to "make up" the low deformation rates that underwent under non slip and increase exponentially the break up of the microstructure in order to reach the fluid transition at the required threshold (bulk yield stress). Clearly then, yielding is strongly correlated to what happens at the wall. The constitutive model though, falls short of predicting the inherent connection between slip and a "steady" hysteretic behaviour of the material, i.e. with slip at the wall the material is truly thixotropic. As it was shown in [38, 39] we can develop models that are thixotropic with or without slip but a different approach has to be taken if the material is thixotropic if slip is present and non-thixotropic when there is no slip at the wall. We believe that the inclusion of a diffusive process in equation (10) will be a step forward into the development of a better understanding of the relation between yielding and slip. This is work that we plan to do in the near future.

7. Acknowledgments

We want to thank the anonymous reviewers, whose useful comments were essential to refining the manuscript.

References

[1] A. M. V. Putz, T. I. Burghelea, The solid-fluid transition in a yield stress shear thinning physical gel, Rheol Acta 48 (2009) 673–689.
[2] B. Y. Han, L. D. Sung, S. W. Kim, Biodegradable block copolymers as injectable drug-delivery systems, Nature 388 (1997) 860–862.
[3] Y. Qiu, K. Park, Environment-sensitive hydrogels for drug delivery, Advanced Drug Delivery Reviews 53 (2001) 321 – 339. Triggering in Drug Delivery Systems.
[4] Q. Hou, P. A. D. Bank, K. M. Shakesheff, Injectable scaffolds for tissue regeneration, J. Matter. Chem. 14 (2004) 1915.
[5] J. Beck, B. Madsen, D. Britt, B. Vernon, K. T. Nguyen, Islet encapsulation: Strategies to enhance islet cell functions, Tissue Engineering 13 (2007) 589–599.
[6] Q. D. Nguyen, D. V. Boger, Measuring the flow properties of yield stress fluids, Annual Review of Fluid Mechanics 24 (1992) 47–88.
[7] P. Coussot, Yield stress fluid flows: A review of experimental data, Journal of Non-Newtonian Fluid Mechanics 211 (2014) 31 – 49.
[8] N. J. Balmforth, I. A. Frigaard, G. Ovarlez, Yielding to stress: Recent developments in viscoplastic fluid mechanics, Annual Review of Fluid Mechanics 46 (2014) 121–146.
[9] D. Bonn, J. Paredes, M. M. Denn, L. Berthier, T. Divoux, S. Manneville, Yield stress materials in soft condensed matter, arXiv:1502.05281 [cond-mat.soft] (2015).
[10] H. A. Barnes, The yield stress–a review or '$\pi\alpha\nu\tau\alpha\ \rho\epsilon\iota$'–everything flows?, Journal of Non-Newtonian Fluid Mechanics 81 (1999) 133–178.
[11] H. A. Barnes, K. Walters, The yield stress myth?, Rheol. Acta 24 (1985) 323–326.
[12] D. Bonn, M. M. Denn, Yield stress fluids slowly yield to analysis, Science 324 (2009) 1401–1402.
[13] M. Denn, D. Bonn, Issues in the flow of yield-stress liquids, Rheologica Acta 50 (2011) 307–315. 10.1007/s00397-010-0504-3.
[14] W. H. Herschel, R. Bulkley, Konsistenzmessungen von gummi-benzollösungen, Kolloid-Zeitschrift 39 (1926) 291–300.
[15] W. Herschel, T. Bulkley, Measurement of consistency as applied to rubbery benzene solutions, Am. Soc. Test Proc. 26 (1926) 621–633.
[16] A. Poumaere, M. Moyers-Gonzalez, C. Castelain, T. Burghelea, Unsteady laminar flows of a carbopol gel in the presence of wall slip, Journal of Non-Newtonian Fluid Mechanics 205 (2014) 28 – 40.
[17] C. Navier, Sur les lois du mouvement des fluides, Mem. Acad. Roy. Sci. Inst. Fr. 6 (1827) 389–440.
[18] M. Kaylon, Dilhan, Apparent slip and viscoplasticity of concentrated suspensions, Journal of Rheology 49 (2005) 621–640.

[19] D. Hill, T. Hasegawa, M. Denn, On the apparent relation between the adhesive failure and melt fracture, J. Rheol. 34 (1990) 891–918.
[20] S. Hatzikiriakos, J. Dealy, Wall slip of molten high density polyethylene. i. sliding plate rheometer studies, J. Rheol. 35 (1991) 497–523.
[21] J. Piau, Carbopol gels: elastoviscoplastic and slippery glasses made of individual swollen sponges: meso- and macroscopic properties, constitutive equations and scaling laws, Journal of Non-Newtonian Fluid Mechanics 144 (2007) 1–29.
[22] J. Piau, N. E. Kissi, Measurement and modelling of friction in polymer melts during macroscopic slip at the wall, Journal of Non-Newtonian Fluid Mechanics 54 (1994) 121–142.
[23] M. Adams, I. Aydin, B. Briscoe, S. Sinha, A finite element analysis of the squeeze flow of an elasto-viscoplastic paste material, Journal of Non-Newtonian Fluid Mechanics 71 (1997) 41–57.
[24] P. Ballesta, G. Petekidis, L. Isa, W. C. K. Poon, R. Besseling, Wall slip and flow of concentrated hard-sphere colloidal suspensions, Journal of Rheology 56 (2012) 1005.
[25] A. Malkin, P. S.A, Wall slip for complex fluids – phenomenon and its causes, Adv. Colloid Interface Sci. 257 (2018) 42–57.
[26] H. Spikes, S. Granick, Equations for slip of simple liquids at smooth solid surfaces, Langmuir 19 (2003) 5065–5071.
[27] G. Kaoullas, G. C. Georgiou, Newtonian poiseuille flows with slip and non-zero slip yield stress, Journal of Non-Newtonian Fluid Mechanics 197 (2013) 24–30.
[28] G. C. Georgiou, G. Kaoullas, Newtonian flow ina triangular duct with slip at the wall, Meccanica 48 (2013) 2577–2583.
[29] N. Roquet, P. Saramito, An adaptive finite element method for viscoplastic flows in a square pipe with stick-slip at the wall, Journal of Non-Newtonian Fluid Mechanics 155 (2008) 101–115.
[30] Y. Damianou, G. C. Georgiou, Viscoplastic poiseuille flow in a rectangular duct with wall slip, Journal of Non-Newtonian Fluid Mechanics 214 (2014) 88–105.
[31] A. S. Yoshimura, R. K. Prud'homme, Response of an elastic bingham fluid to oscillatory shear, Rheologica Acta 26 (1987) 428–436.
[32] L. Fusi, A. Farina, F. Rosso, Flow of a bingham-like fluid in a finite channel of varying width: A two-scale approach, Journal of Non-Newtonian Fluid Mechanics 177-178 (2012) 76–88.
[33] L. Fusi, A. Farina, F. Rosso, Squeeze flow of a bingham-type fluid with elastic core, International Journal of Non-Linear Mechanics 78 (2016) 59–65.
[34] A. M. V. Putz, T. I. Burghelea, I. A. Frigaard, D. M. Martinez, Settling of an isolated spherical particle in a yield stress shear thinning fluid., Phys. Fluids (2008) 033102.
[35] T. Divoux, V. Grenard, S. Manneville, Rheological hysteresis in soft glassy materials, Phys. Rev. Lett. 110 (2013) 018304.
[36] Z. Kebiche, C. Castelain, T. Burghelea, Experimental investigation of the rayleigh–bénard convection in a yield stress fluid, Journal of Non-Newtonian Fluid Mechanics 203 (2014) 9 – 23.
[37] M. M. Gonzalez, T. Burghelea, J. Mak, Linear stability analysis for plane-poiseuille flow of an elastoviscoplastic fluid with internal microstructure for large reynolds numbers, Journal of Non-Newtonian Fluid Mechanics 166 (2011) 515 – 531.
[38] R. Sainudiin, M. Moyers-Gonzalez, T. Burghelea, A microscopic gibbs field model for the macroscopic yielding behaviour of a viscoplastic fluid, Soft Matter 11 (27) (2015) 5531–5545.
[39] T. Burghelea, M. Moyers-Gonzalez, R. Sainudiin, A nonlinear dynamical system approach for the yielding behaviour of a viscoplastic material, Soft Matter 13 (2017) 2024–2039.
[40] E. Weber, M. Moyers-González, T. I. Burghelea, Thermorheological properties of a Carbopol gel under shear, Journal of Non-Newtonian Fluid Mechanics 183 -184 (2012) 14 – 24.
[41] D. Tarlet, E. Younes, S. Roux, A. Levy, T. Burghelea, Stopping of a solid object in an elasto viscoplastic material, Journal of Non-Newtonian Fluid Mechanics 263 (2019) 120 – 129.
[42] M. Dinkgreve, M. Fazilati, M. M. Denn, D. Bonn, Carbopol: From a simple to a thixotropic yield stress fluid, Journal of Rheology 62 (2018) 773–780.
[43] P. Coussot, Q. D. Nguyen, H. T. Huynh, D. Bonn, Avalanche behavior in yield stress fluids, Phys. Rev. Lett. 88 (2002) 175501.
[44] R. Sainudiin, M. Moyers-Gonzalez, T. Burghelea, A microscopic gibbs field model for the macroscopic behavior of a viscoplastic fluid, UCDMS Research Report 2014/1 (2014) 1–17.
[45] P. Coussot, Rheometry of pastes, suspensions and granular materials, John Willey & Sons, 2005.
[46] G. Ovarlez, S. Cohen-Addad, K. Krishan, J. Goyon, P. Coussot, On the existence of a simple yield stress fluid behavior, Journal of Non-Newtonian Fluid Mechanics 193 (2013) 68 – 79.